

Tailoring Bulk Photovoltaic Effects in Magnetic Sliding Ferroelectric Materials

Chunmei Zhang¹, Ping Guo¹, Jian Zhou^{2,*}

¹School of Physics, Northwest University, Xi'an 710069, China

²Center for Alloy Innovation and Design, State Key Laboratory for Mechanical Behavior of Materials, Xi'an Jiaotong University, Xi'an 710049, China

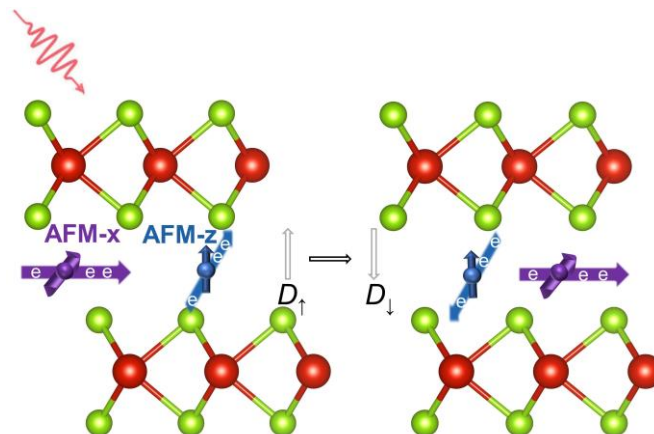
*Email: jianzhou@xjtu.edu.cn

Abstract

The bulk photovoltaic effect that is intimately associated with crystalline symmetry has been extensively studied in various nonmagnetic materials, especially ferroelectrics with a switchable electric polarization. In order to further engineer the symmetry, one could resort to spin-polarized systems possessing an extra magnetic degree of freedom. Here, we investigate the bulk photovoltaic effect in two-dimensional magnetic sliding ferroelectric (MSFE) systems, illustrated in VSe_2 , $FeCl_2$, and CrI_3 bilayers. The transition metal elements in these systems exhibit intrinsic spin polarization, and the stacking mismatch between the two layers produce a finite out-of-plane electric dipole. Through symmetry analyses and first-principles calculations, we show that photoinduced in-plane bulk photovoltaic current can be effectively tuned by their magnetic order and the out-of-plane dipole moment. The underlying mechanism is elucidated from the quantum metric dipole distribution in the reciprocal space. The ease of the fabrication and manipulation of MSFEs guarantee practical optoelectronic applications.

Keywords: bulk photovoltaic effect, symmetry constraints, magnetic sliding ferroelectrics, $\mathbf{k}\cdot\mathbf{p}$ model, first-principles calculations

TOC figure



Bulk photovoltaic (BPV) effect, a second order nonlinear optical (NLO) response, could produce steady-state electric current under homogeneous optical illumination.¹⁻³ According to theoretical estimations, it may host the potential to overpass the well-known Shockley-Queisser limit in conventional solar cells, yet one does not require complicated p - n heterojunction fabrications for the photo-electric conversion.⁴ Fundamentally, the BPV process serves as an efficient tool for detecting the electronic topology.⁵ Extensive studies on BPV effect in time-reversal (\mathcal{T}) invariant systems have been conducted, including their shift current,⁶⁻⁸ injection current,⁹ nonlinear Hall current generations,¹⁰ etc.¹¹ They are rooted in various geometric phases of the electronic wavefunctions, namely, shift vector, Berry connection, and Berry curvature dipole, respectively. These features assign that the BPV currents only emerge in centrosymmetry (\mathcal{P}) broken systems, e.g., ferroelectric materials.¹²⁻¹⁵

Two-dimensional (2D) materials are attractive for their good optical accessibility, compared with the conventional 3D bulk systems, as their ultrahigh surface-to-volume ratio and marginal light dispersion vertical to the atomic plane. As such, the phase-matching condition in NLO processes (e.g., second harmonic generation) is naturally satisfied. Over the past decade, several 2D ferroelectric materials have been theoretically predicted and then realized in subsequent experiments, such as group-IV monochalcogenides,¹⁶ In₂Se₃ monolayer,¹⁷ CuInP₂S₆ ultrathin flakes,¹⁸ BiFeO₃ in one unit-cell thick,¹⁹ d 1T-MoTe₂ monolayer,²⁰ etc. Nonetheless, the scarcity of intrinsic 2D ferroelectric systems limits their practical usage, and other routes to introducing electric dipoles need further exploration. Recently, Wu *et al.* proposed the concept of interfacial ferroelectricity in 2D van der Waals (vdW) materials, which could generate sizable out-of-plane dipole moments (D_z) in multilayer forms that are non-ferroelectric in their monolayer counterparts.²¹⁻²² The flipping of D_z (between D_\uparrow and D_\downarrow) can be done via a short distance shuffling or sliding between neighboring vdW layers. Hence, they are referred to as sliding ferroelectric (SFE) materials.²³⁻²⁶ Owing to the low energy barrier (~ 0.1 $\mu\text{J}/\text{cm}^2$) separating the D_\uparrow and D_\downarrow states, the flipping could occur in an ultrafast kinetics with high contrast. This motivates various experimental investigations after the theoretical predictions, and several SFEs have been demonstrated in h -BN, H and T' phases of transition metal dichalcogenides, etc.^{20, 27}

The out-of-plane dipole moment in SFE bilayers constraints that only nonlinear Hall current can be switched under D_z flipping, while both in-plane shift and injection currents maintain their direction and magnitude.²⁸⁻²⁹ In order to further toggle the BPV currents in SFEs, we propose that breaking \mathcal{T} -symmetry is an efficient way which adds another tuning parameter, namely, magnetic order (spin polarization direction). The interplay between different ferroic orders, such as ferromagnetism and ferroelectricity, has led to tremendous exotic physical properties with novel

applications.³⁰⁻³¹ Here both spin and electric polarizations offer large space to engineer the symmetry, thus the light-matter interaction in the magnetic ferroelectric materials would provide additional manipulation opportunities for the BPV current generations.³²

Recently, it has been shown that in magnetic systems the normal BPV (shift and injection) currents could exhibit magnetic counterparts, which vanish in nonmagnetic materials.³³ These magnetic cousins are dubbed magnetic shift current and magnetic injection current (MIC), arising from the inequivalent distribution of the Kramers pair states at \mathbf{k} and $-\mathbf{k}$.³⁴ Several NLO investigations in magnetic systems have been carried out, and special care has been given to \mathcal{PT} -symmetry, e.g., antiferromagnetic (AFM) bilayer CrI_3 and MnBi_2Te_4 .^{32,34-36} In such cases, the normal shift current (NSC) and normal injection current diminish. In this Letter, we consider magnetic SFE (referred to as MSFE) systems, in which all the \mathcal{P} , \mathcal{T} , and \mathcal{PT} symmetries are broken. Thus, they host both normal and magnetic BPV currents simultaneously. The tunability of magnetic order and electric dipole provide a vast space for the BPV current manipulation.

We use H-VSe₂ and T-FeCl₂ bilayers to illustrate this concept, and perform first-principles density functional theory (DFT) calculations to evaluate the BPV photoconductivity. Note that in the discovery of both low-dimensional magnetic materials and SFE concepts, theoretical approaches (mainly according to DFT calculations) have shown its powerful predicting ability with good accuracy. These prior calculations have evoked several subsequent experimental investigations, e.g., monolayer VSe₂,³⁷⁻³⁸ CrI₃,³⁹⁻⁴¹ Fe₃GeTe₂,⁴²⁻⁴³ CrSBr,⁴⁴⁻⁴⁵ MnSe₂,⁴⁶⁻⁴⁷ etc.^{22-23,28,48-51} According to previous theoretical works, both H-VSe₂⁵²⁻⁵³ and T-FeCl₂⁵⁴ can be physically exfoliated from their bulk counterparts. They belong to hexagonal lattice and exhibit good chemical and thermodynamic stability. Their optimal bilayer stacking induces finite interfacial D_z . The unfilled d orbitals in the transition metals produce intrinsic magnetic polarizations, giving intralayer ferromagnetic (FM) and interlayer AFM configuration. These ensure that their bilayers belong to MSFE materials, where the magnetic order vector ($\mathbf{L} = \mathbf{M}_1 - \mathbf{M}_2$, \mathbf{M} being magnetic vector in each layer) and electric polarization D_z can be efficiently controlled and modulated. We show that under linearly polarized light (LPL) irradiation, the MIC generation depends on both \mathbf{L} and D_z . On the other hand, the LPL induced NSC remains in its direction regardless of \mathbf{L} and D_z . Since the flow directions of NSC and MIC under certain magnetic cases are vertical to each other, these photocurrents can be individually detected and controlled without strong entanglement.

Geometric and electronic properties of MSFEs. All monolayers H-VSe₂⁵⁵, T-FeCl₂⁵⁶ and CrI₃ belong to hexagonal lattice. Similar as that in the monolayer MoS₂,⁵¹ there are several SFE stacking configurations. In the main text, we will mainly focus on the H-VSe₂, while leaving results and discussions for the T-FeCl₂ and CrI₃ in Supporting Information (SI). In Figure 1a, we plot the

atomic structures of a high symmetric VSe₂ bilayer, where the upper layer is eclipsed over the lower one. This is denoted as the intermediate (IM) state, as it is energetically unstable and would spontaneously slide into two energetically degenerate patterns, namely, D_{\uparrow} (Figure 1b) and D_{\downarrow} (Figure 1c). Our calculation shows their dipole moment to be $\pm 0.078 \mu\text{C}/\text{cm}^2$, larger than the experimentally observed values of $0.032 \mu\text{C}/\text{cm}^2$ in bilayer WTe₂.⁵⁷ The D_{\uparrow} and D_{\downarrow} states are subject to an in-plane sliding $t\left(\frac{1}{3}, \frac{2}{3}, 0\right)$ and $t\left(\frac{2}{3}, \frac{1}{3}, 0\right)$ (direct coordinates relative to lattice) from IM, respectively, and the switching entails an energy barrier of 64 meV per formula unit (f.u.), comparable to that of the In₂Se₃ monolayer (66 meV/f.u.).⁵⁸

One notes that each Se favors a formal -2 reduction state, so that the V atom is in its $+4$ oxidation state. Therefore, each V leaves one unpaired electron, carrying $\sim 1 \mu_{\text{B}}$ local magnetic moment. As elucidated previously,^{38,59} the monolayer VSe₂ exhibits (intralayer) FM semiconducting ground state, with the valence band maximum (VBM) and conduction band minimum (CBM) locating at K and K' in the first Brillouin zone (BZ). When two VSe₂ layers are stacked, the interlayer coupling prefers AFM configuration, which is energetically lower than the FM interlayer state by 3 meV per unit cell. Our calculation results are well consistent with previous works.⁶⁰ We tabulate these results in Table S1. In this regard, the VSe₂ bilayer conceives both electric and magnetic polarizations simultaneously, making it a type-I multiferroic system.

The calculated band structures in different patterns are plotted in Figures 1d–1f. We assign the magnetic order \mathbf{L} along z (denoted as $\mathbf{L} \parallel \hat{\mathbf{z}}$). One sees that all of them exhibit an indirect bandgap semiconducting feature with both valence and conduction bands near the Fermi level mainly contributed by the V- d orbitals. The VBM of the IM state at the K and K' valleys are energetically degenerate and contributed by the upper (spin up) and lower (spin down) layer, respectively (Figure 1d). This is because that the two layers can be mapped through a mirror reflection \mathcal{M}_z multiplying \mathcal{T} , which gives eigenenergy $E(\mathbf{k}, \text{spin up}) = E(-\mathbf{k}, \text{spin down})$. Under finite D_z , the built-in electric potential lifts such degeneracy (\mathcal{M}_z -broken). According to our calculations, a large valley polarization of ~ 70 meV can be observed in the two MSFE states (Figures 1e and 1f). Compared with experimentally observed valley splitting of tens of meV in SiO₂/Si(100)/SiO₂ quantum well^{61–62} and 2.5 meV under the magnetic field of 1 Tesla in WSe₂ monolayer,⁶³ such valley polarization is significant enough to be observed.

One can understand such valley polarization in the $\mathbf{L} \parallel \hat{\mathbf{z}}$ VSe₂ MSFE using a simplified $\mathbf{k}\cdot\mathbf{p}$ model,

$$H = H_0 + H'_D + H'_{SOC} = H_0 + \lambda_z D_z \sigma_z + \lambda_{SOC} (3k_x^2 - k_y^2) k_y \sigma_z. \quad (1)$$

Here, H_0 contains crystal field and magnetic exchange effect in the system, which is essentially the

Hamiltonian of the IM state without SOC interactions. H'_D is the electronic splitting induced by D_z , and the H'_{SOC} is the SOC triggered spin splitting up to cubic \mathbf{k} -terms in the C_{3v} system.⁶⁴ The wrapping term is included only because the Rashba SOC is associated with the in-plane spin polarization. The σ_z is the z -component Pauli matrix for spin. λ_z and λ_{SOC} refer to the D_z -spin coupling strength and the intrinsic SOC strength, respectively.

The D_z serves as an effective magnetic field that couples with spin and lifts the spin degeneracy, i.e., the reversal of D_z flips spin up and spin down states (Figure S1). One also notes that H'_{SOC} splits spin degeneracy at the K and K' valley. Thus, the synergistic effects of D_z and SOC result in the valley polarization of the D_\uparrow and D_\downarrow bilayer VSe₂ ($\mathbf{L} \parallel \hat{\mathbf{z}}$), and the magnitude scales with λ_z and λ_{SOC} (Figure S1). Remarkably, the dipole moment induces layer-imbalanced wavefunction distributions at any generic momenta pair (\mathbf{k} and $-\mathbf{k}$), which play a vital role in the injection photocurrent generation.

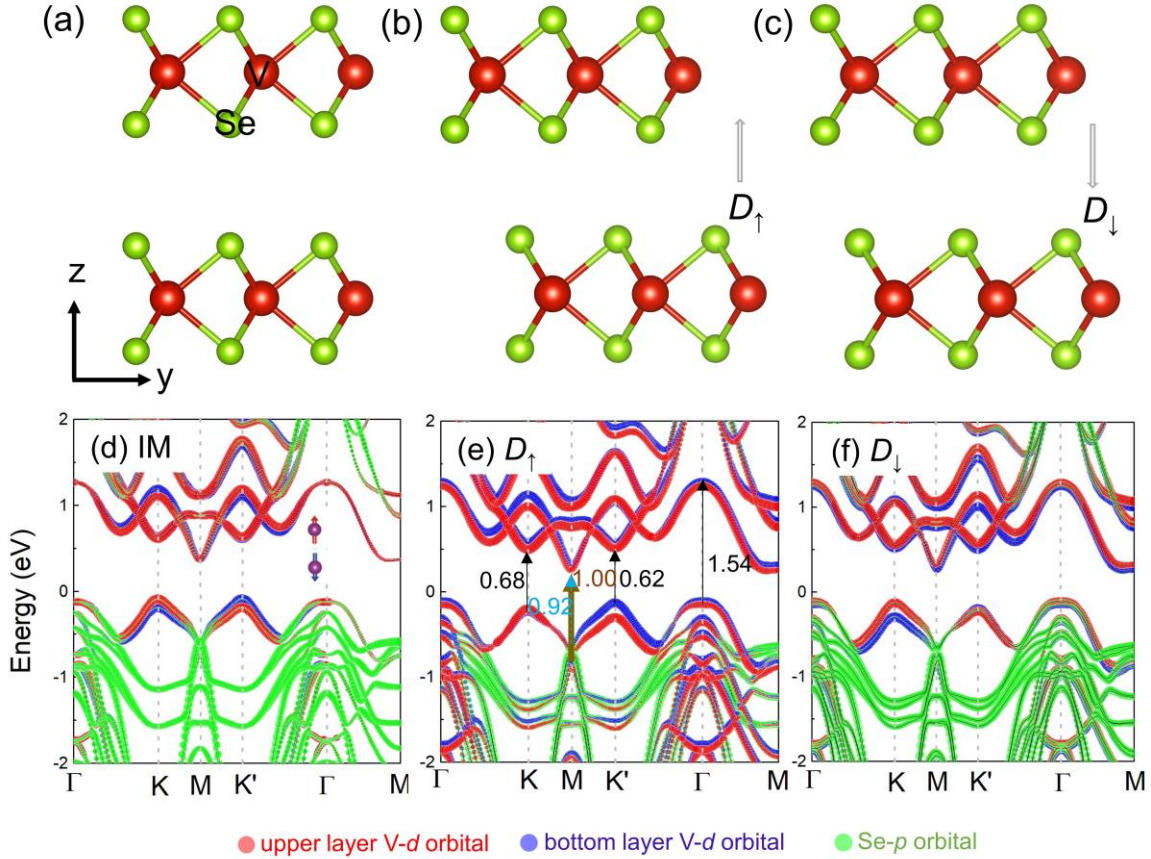


Figure 1. Atomic geometry of the (a) IM, (b) D_\uparrow , and (c) D_\downarrow stacking patterns of bilayer VSe₂. (d)–(f) Calculated band structures for the IM, D_\uparrow , and D_\downarrow states ($\mathbf{L} \parallel \hat{\mathbf{z}}$). The energy is relative to the Fermi level. Values in panel (e) measure the direct bandgaps (in eV) at different \mathbf{k} points.

Symmetry considerations of photoconductivity. We show that the symmetry of MSFE VSe₂ bilayer is very sensitive to \mathbf{L} and D_z , which could switch the BPV photocurrents. Particularly,

according to previous works,³⁴ LPL would induce both NSC and MIC generations. Note that for \mathcal{T} -symmetric systems, MIC vanishes, while NSC is symmetrically forbidden for \mathcal{PT} -systems. Both of them may exist in general cases, which is the situation in the MSFEs as studied here. Hence, we will consider both NSC and MIC generations, which carry geometric phases of electric wavefunctions, namely, shift vector and quantum metric dipoles (see Methods section).^{10, 65-66}

The NSC and MIC photocurrent densities are³⁴

$$J_{\text{NSC}}^a = \sigma^{abb}(0; \omega, -\omega)E_b(\omega)E_b(-\omega), \quad (2)$$

$$J_{\text{MIC}}^a = \eta^{abb}(0; \omega, -\omega)E_b(\omega)E_b(-\omega). \quad (3)$$

Here, the σ^{abb} and η^{abb} are the photoconductivity for NSC and MIC, respectively. E is the alternating electric field (with angular frequency ω), and a (b) refers to Cartesian coordinate in the xy plane. Even though the higher order photo-responses would present as well. We note that when the light intensity is not significant, the photocurrent would reduce as the nonlinear order increases, according to the Kubo perturbation theory.^{5, 67} Also, one notes that the static photocurrent does not exist for the third order photo-responses under a monochromatic light irradiation. In this regard, we only focus on the second order BPV effect in the current work.

According to the atomic coordination (ignoring spin polarization), the IM pattern belongs to the crystalline layer group $P\bar{6}m2$, which includes two mirror reflections with their normal direction along x (\mathcal{M}_x) and z (\mathcal{M}_z). The D_\uparrow and D_\downarrow states break \mathcal{M}_z , belonging to the layer group of $P3m1$. When we include spin polarization effect, the \mathcal{M}_x becomes $\mathcal{M}_x\mathcal{T}$ for the $\mathbf{L} \parallel \hat{\mathbf{z}}$, since spin transforms as a pseudovector. For the IM state, the \mathcal{M}_z changes into $\mathcal{M}_z\mathcal{T}$. However, if the magnetic moment on V switches its direction, such symmetry constraints would alter. For example, in the $\mathbf{L} \parallel \hat{\mathbf{x}}$ case, one has \mathcal{M}_x reflection for all the three sliding structures, while the IM state contains \mathcal{M}_z . The $\mathbf{L} \parallel \hat{\mathbf{y}}$ configuration is different, which needs multiplication of \mathcal{T} onto \mathcal{M}_x (for all three patterns). We list these symmetries in Table 1.

Next, we move to the symmetry constraints for NSC and MIC photoconductivities under LPL. According to Eq. (5) (see Methods), the NSC is defined as the overall contribution of shift vectors weighted by the absorption rate in the whole BZ.⁶⁸ As the absorption rate is always positive, the direction of the σ^{abb} is scaled by the shift vector R_{mn}^a ,⁶⁹ which transforms as a polar vector, giving that $\mathcal{M}_x R_{nm}^x(k_x, k_y) = -R_{nm}^x(-k_x, k_y)$ and is immune to \mathcal{T} . Hence, the σ^{xxx} and σ^{xyy} are symmetrically forbidden, leaving only σ^{yxx} and σ^{yyy} to be finite.

To check whether the direction of the NSC could be tuned by the dipole moment D_z , we further analyze the structure relationship between D_\uparrow and D_\downarrow . Ignoring the spin order, the D_\uparrow and D_\downarrow spatial

patterns are related to each other by $\mathcal{M}_z D_\uparrow = D_\downarrow$. The direction of the σ^{abb} is controlled by the in-plane shift vector R_{mn}^a ,⁶⁹ which does not flip sign upon the out-of-plane FE transition, $\mathcal{M}_z R_{mn}^a = R_{mn}^a$. Thus, the NSC keeps its direction regardless of D_z and \mathbf{L} .

As for the MIC generation, we show that \mathbf{L} strongly affects the symmetry assignments. According to the Kubo perturbation theory and previous works,³⁴ the MIC arises from an excitation from bands m to n with the quantum metric tensor g_{nm}^{bb} , weighted by the asymmetric group velocity difference Δ_{nm}^a at $\pm\mathbf{k}$ (see Methods). The symmetry transformation gives $\mathcal{T}\Delta^a(\mathbf{k}) = -\Delta^a(-\mathbf{k})$ and $\mathcal{M}_x\Delta^a(\mathbf{k}) = (-1)^{\delta_{xa}}\Delta^a(\tilde{\mathbf{k}})$, where $\tilde{\mathbf{k}} = (-k_x, k_y)$.⁷⁰ The quantum metric g_{nm}^{bb} transforms as $\mathcal{T}g_{nm}^{bb}(\mathbf{k}) = g_{nm}^{bb}(-\mathbf{k})$ and $\mathcal{M}_x g_{nm}^{bb}(\mathbf{k}) = g_{nm}^{bb}(\tilde{\mathbf{k}})$. Therefore, under (x or y -polarized) LPL, for the D_\uparrow and D_\downarrow states, the MIC always transports along the y direction for $\mathbf{L} \parallel \hat{\mathbf{x}}$, while it flows along the x direction for $\mathbf{L} \parallel \hat{\mathbf{y}}$ and $\mathbf{L} \parallel \hat{\mathbf{z}}$ situations.

For the $\mathbf{L} \parallel \hat{\mathbf{x}}$ and $\mathbf{L} \parallel \hat{\mathbf{y}}$ IM states, the mirror- z reflection assigns constraints on the velocity difference as $\mathcal{M}_z\Delta^a(\mathbf{k}) = \Delta^a(\mathbf{k})$. Thus, they give similar MIC directions with those in both D_\uparrow and D_\downarrow (flowing along x and y , respectively). When it comes to the $\mathbf{L} \parallel \hat{\mathbf{z}}$ IM state, the symmetry constraint becomes $\mathcal{M}_z\mathcal{T}\Delta^a(\mathbf{k}) = -\Delta^a(-\mathbf{k})$, which diminishes both η^{xxx} and η^{xyy} . Thus, the existence of $\mathcal{M}_z\mathcal{T}$ results in symmetric distribution and opposite sign of the $\Delta_{nm}^x g_{nm}^{xx}$ at \mathbf{k} and $-\mathbf{k}$, so that J_{MIC}^{xbb} is strictly to be zero. Accordingly, for the D_\uparrow and D_\downarrow states, the removal of $\mathcal{M}_z\mathcal{T}$ gives non-vanishing J_{MIC}^{xbb} .³² These symmetric results for the MIC are listed in Table 1. In this table, the allowed (nonzero) MIC are given under each operation. In addition, the presence or absence of the MIC can also be estimated from the asymmetric bands at \mathbf{k} and $-\mathbf{k}$, as shown in Figure S2.

Table 1. Magnetization orientation dependent symmetry operations and the allowed MIC for the IM, D_\uparrow , and D_\downarrow states. We only list the AFM interlayer configuration results, and the symmetry analyses for the FM interlayer structures are shown in Table S2. Note that this is only valid for bilayer MSFEs (or even layer numbered MSFEs), while the trilayer (or odd layer numbered) MSFEs are different (see Figure S3 and Table S3 in SI).

	D_\uparrow and D_\downarrow		IM	
	Symmetry	Allowed photocurrents	Symmetry	Allowed photocurrents
$\mathbf{L} \parallel \hat{\mathbf{x}}$	\mathcal{M}_x	η^{yyy}, η^{yxx}	$\mathcal{M}_x, \mathcal{M}_z$	η^{yyy}, η^{yxx}
$\mathbf{L} \parallel \hat{\mathbf{y}}$	$\mathcal{M}_x\mathcal{T}$	η^{xxx}, η^{xyy}	$\mathcal{M}_x\mathcal{T}, \mathcal{M}_z$	η^{xxx}, η^{xyy}
$\mathbf{L} \parallel \hat{\mathbf{z}}$	$\mathcal{M}_x\mathcal{T}$	η^{xxx}, η^{xyy}	$\mathcal{M}_x\mathcal{T}, \mathcal{M}_z\mathcal{T}$	all forbidden

We show that D_z can be used to control the direction and magnitude of MIC for the $\mathbf{L} \parallel \hat{\mathbf{z}}$ configuration. This can be understood by noting that the D_\uparrow and D_\downarrow states are connected via $\mathcal{M}_z \mathcal{T} D_\uparrow = D_\downarrow$. Thus, the transformation between $\eta_{D_\uparrow}^{xxx}$ and $\eta_{D_\downarrow}^{xxx}$ (for $\mathbf{L} \parallel \hat{\mathbf{z}}$) satisfies

$$\begin{aligned} \eta_{D_\downarrow}^{xxx} &= \mathcal{M}_z \mathcal{T} \eta_{D_\uparrow}^{xxx} \sim \mathcal{M}_z \mathcal{T} \sum_{mn, \mathbf{k}} f_{nm}(\mathbf{k}) \Delta_{nm}^x(\mathbf{k}) g_{nm}^{xx}(\mathbf{k}) \delta(\omega_{mn}(\mathbf{k}) - \omega) \\ &= - \sum_{mn, -\mathbf{k}} f_{nm}(-\mathbf{k}) \Delta_{nm}^x(-\mathbf{k}) g_{nm}^{xx}(-\mathbf{k}) \delta(\omega_{mn}(-\mathbf{k}) - \omega) \\ &= - \sum_{mn, \mathbf{k}} f_{nm}(\mathbf{k}) \Delta_{nm}^x(\mathbf{k}) g_{nm}^{xx}(\mathbf{k}) \delta(\omega_{mn}(\mathbf{k}) - \omega) \sim - \eta_{D_\uparrow}^{xxx} = \eta_{D_\downarrow}^{xxx}. \end{aligned} \quad (4)$$

Here, the product of $g_{nm}^{bb}(\mathbf{k}) \delta(\omega_{mn} - \omega)$ measures the light absorption rate of each \mathbf{k} point. This suggests that the MIC direction can be well-controlled by D_z in the MSFE bilayer, which is significantly different from the nonmagnetic SFE bilayers²⁹ that vertical dipole flip keeps the photocurrent unchanged.

Similar behavior can be found in the $\mathbf{M} \parallel \hat{\mathbf{x}}$ and $\mathbf{M} \parallel \hat{\mathbf{y}}$ interlayer configurations of FM interlayer configuration (\mathbf{M} denotes the spin polarization vector), as they share the same structural symmetry transformation rules with that of $\mathbf{L} \parallel \hat{\mathbf{z}}$. While for other magnetic configurations ($\mathbf{L} \parallel \hat{\mathbf{x}}$, $\mathbf{L} \parallel \hat{\mathbf{y}}$, and $\mathbf{M} \parallel \hat{\mathbf{z}}$), the D_\uparrow and D_\downarrow states are related to each other by \mathcal{M}_z . Hence, the MIC is unchanged under D_z reversal. In this way, the MIC provides a facile way to detect the electric and magnetic configurations in MSFEs.

First-principles calculation results. In order to verify the above symmetry conclusions and quantify the photoconductivity, we perform first-principles DFT calculations. First of all, our magnetocrystalline anisotropy energy (MAE) calculation including full SOC effect shows that the magnetic moment prefers lying in the xy plane, while the $\mathbf{L} \parallel \hat{\mathbf{z}}$ is ~ 2 meV/f.u. higher in energy. This indicates that VSe₂ monolayer belongs to XY magnetic model, which could exhibit Berezinskii–Kosterlitz–Thouless (BKT) transition. This infers that the experimental measurements should be performed under low temperature, as in the observation of the CrCl₃ monolayer.⁷¹ The in-plane MAE can be broken when one resorts to uniaxial strains, or carefully selecting specific substrate with strong anisotropy. The detailed results are shown in Figure S4, Tables S4 and S5. In addition, previous works have suggested that an external electric field can induce magnetoelectric Edelstein effect,⁷²⁻⁷⁴ which could generate a sufficiently large effective magnetic field. In this way, the system could belong to the Ising model with fixed magnetic easy axis, aiding the potential experimental verifications of long-range magnetism.

The NSC is unaffected by \mathcal{T} and D_z , which transports along y in all these cases (Figure 2, Figures S5 and S6). These results totally agree with the previous symmetry analyses. In the $\mathbf{L} \parallel \hat{\mathbf{z}}$ case, the \mathcal{M}_x and \mathcal{C}_3 rotation symmetries lead to one independent in-plane non-vanishing shift

current tensor, $\sigma^{yyy} = -\sigma^{yxx}$. From Figure 2, we see that finite NSC is generated across a large energy range due to the interband optical excitation above the bandgap. Thus, above bandgap open-circuit voltage is generated. The maximum value of σ^{yyy} reaches $28 \mu\text{A}/\text{V}^2$ at an incident light energy of 1.6 eV. Compared with previously proposed 2H-MoS₂ monolayer (photoconductivity $8 \mu\text{A}/\text{V}^2$ at the photon energy of 2.8 eV),⁷⁵ the σ^{yyy} in MSFE bilayer VSe₂ is much larger.

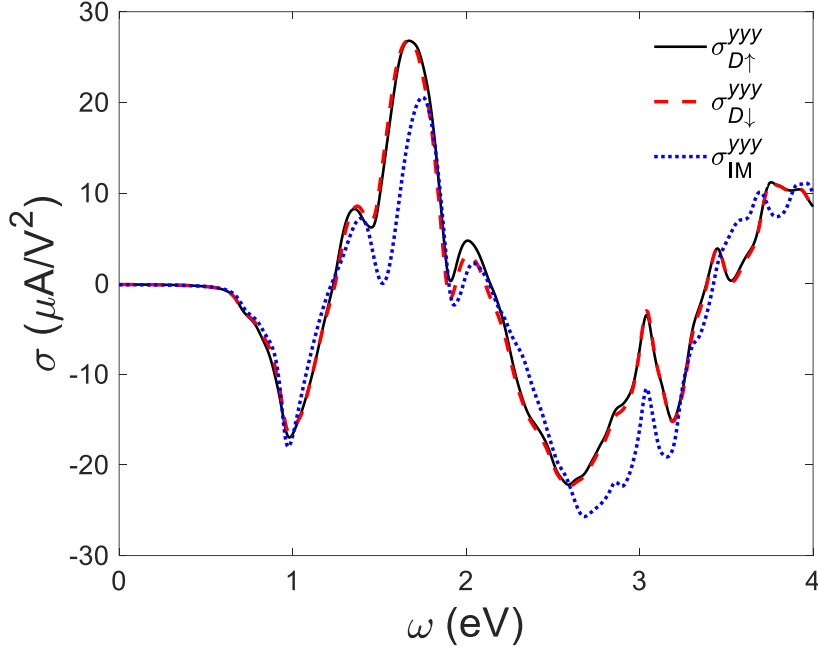


Figure 2. Incident light photon energy dependent NSC photoconductivities in the $\mathbf{L} \parallel \hat{\mathbf{z}}$ IM, D_{\uparrow} , and D_{\downarrow} states of bilayer VSe₂. One sees that flipping the dipole keeps the NSC.

Figures 3a and 3b depict the MIC photoconductivity of η_{IM} , $\eta_{D_{\uparrow}}$, and $\eta_{D_{\downarrow}}$ for the $\mathbf{L} \parallel \hat{\mathbf{x}}$, and those for $\mathbf{L} \parallel \hat{\mathbf{y}}$ are shown in Figures 3c and 3d. Consistent with previous symmetry results, for the $\mathbf{L} \parallel \hat{\mathbf{x}}$, only the y -direction MIC survives. Rotating the magnetic axis to y ($\mathbf{L} \parallel \hat{\mathbf{y}}$) switches the MIC direction to x . This demonstrates that magnetic order \mathbf{L} strongly affects the MIC feature. It should be noted that the $\mathbf{L} \parallel \hat{\mathbf{y}}$ magnetization yields vertically propagating NSC and MIC, which could be detected and measured separately. In both the $\mathbf{L} \parallel \hat{\mathbf{x}}$ and $\mathbf{L} \parallel \hat{\mathbf{y}}$ cases, flipping D_z maintains the MIC. The magnitude of η reaches $10 \mu\text{A}/\text{V}^2$, when we assume the carrier lifetime τ to be 0.1 ps. This carrier lifetime accounts for the scattering that arises from the environment such as temperature, disorder, impurities, etc. Note that even though the carrier lifetime essentially depends on band index and momentum, a rigorous evaluation is not straightforward. Hence, we follow the conventional approach to adopt a universal value.¹¹ Compared to experimental measurements and theoretical estimations, e.g., 0.4 ps for CrI₃³² and 0.2 ps for Ge,⁷⁶⁻⁷⁷ our choice of 0.1 ps is conservative and may not overestimate the injection current magnitude. The MIC photoconductivity value indicates that under a LPL irradiation with its electric field magnitude of 3 V/nm, one could

generate a current density of $90 \mu\text{A}/\text{nm}^2$. Note that here we assume the effective thickness of VSe_2 bilayer to be 0.96 nm , which is estimated from its corresponding bulk structure.

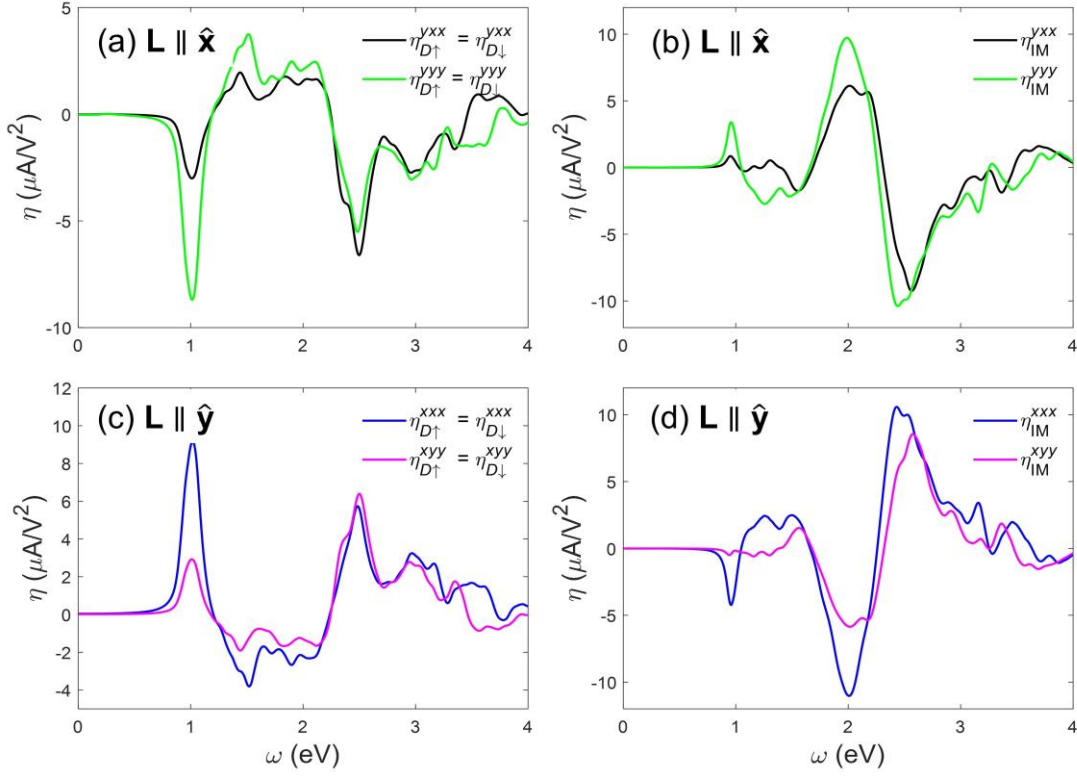


Figure 3. MIC for (a), (b) $\mathbf{L} \parallel \hat{\mathbf{x}}$ and (c), (d) $\mathbf{L} \parallel \hat{\mathbf{y}}$ of bilayer VSe_2 . Both x - and y -LPL results are shown.

When the magnetization is along the z -axis, the MIC flowing along y is symmetrically forbidden. In this case, the system preserves \mathcal{C}_3 rotation. Hence, the x and y -LPL generate opposite MIC (Figure 4a), namely, $\eta^{xxx} = -\eta^{xyy}$ for both the D_\uparrow and D_\downarrow states. The MIC magnitude reaches $\sim 2.8 \mu\text{A}/\text{V}^2$ at the incident photon energy of $\sim 1 \text{ eV}$ ($\tau = 0.1 \text{ ps}$). In addition, flipping the MSFE dipole reverses the MIC, $\eta_{D_\uparrow}^{xbb} = -\eta_{D_\downarrow}^{xbb}$ ($b = x$ or y). In the IM pattern, the MIC is symmetrically forbidden. These are well-consistent with our previous symmetry arguments. The frequency-dependent MIC photoconductivity responses for the FM configurations are shown in Figure S7. All these results demonstrate that the direction of the MIC can be controlled by \mathbf{L} and D_z .

To further enlighten the absence and presence of the MIC and its D_z control in the $\mathbf{L} \parallel \hat{\mathbf{z}}$ bilayer VSe_2 , we plot the BZ contribution of η^{xxx} with the incident photon energy of 1 eV (Figures 4b–4d). One sees that the main contributions are from the vicinity of the M point, which arises from the electron transition between the Se- p (VB-3) and V- d (CB) orbitals (Figure 1e). The \mathbf{k} -resolved Δ_{nm}^x , g_{nm}^{bb} , and $\Delta_{nm}^x g_{nm}^{xx}$ distributions in the BZ for IM, D_\uparrow and D_\downarrow states are presented in Figure S8 and Figures 4b-d. For the IM state, it is evident that equally positive and negative proportion of the

quantum metric dipole in BZ, $\Delta_{nm}^x(k_x, k_y)g_{nm}^{xx}(k_x, k_y) = -\Delta_{nm}^x(-k_x, -k_y)g_{nm}^{xx}(-k_x, -k_y)$, leading to cancellation of the η^{xxx} .³² However, for the D_\uparrow and D_\downarrow , one sees that the quantum metric dipole distributes inequivalently under $\mathbf{k} \rightarrow -\mathbf{k}$. For example, the positive quantum metric dipole at $(-k_x, -k_y)$ around M surpasses that of the negative one at (k_x, k_y) for D_\uparrow . This feature is reversed for D_\downarrow . Hence, the asymmetric quantum metric dipole in the BZ generates nonvanishing current. In addition, the opposite quantum metric dipole distributions for D_\uparrow and D_\downarrow reverse the sign of η^{xxx} .

One should note that the amount of \mathbf{k} to $-\mathbf{k}$ symmetry breaking reflects the intensity of the MIC. According to our low energy model, the synergistic effects of H'_D and H'_{SOC} lead to valley polarization and asymmetric wavefunction distribution between \mathbf{k} and $-\mathbf{k}$. Hence, both the parameters λ_z and λ_{SOC} control the MIC magnitude. In order to yield enhanced MIC photoconductivity, one could resort to materials that possess large sliding dipole moments with heavy elements.

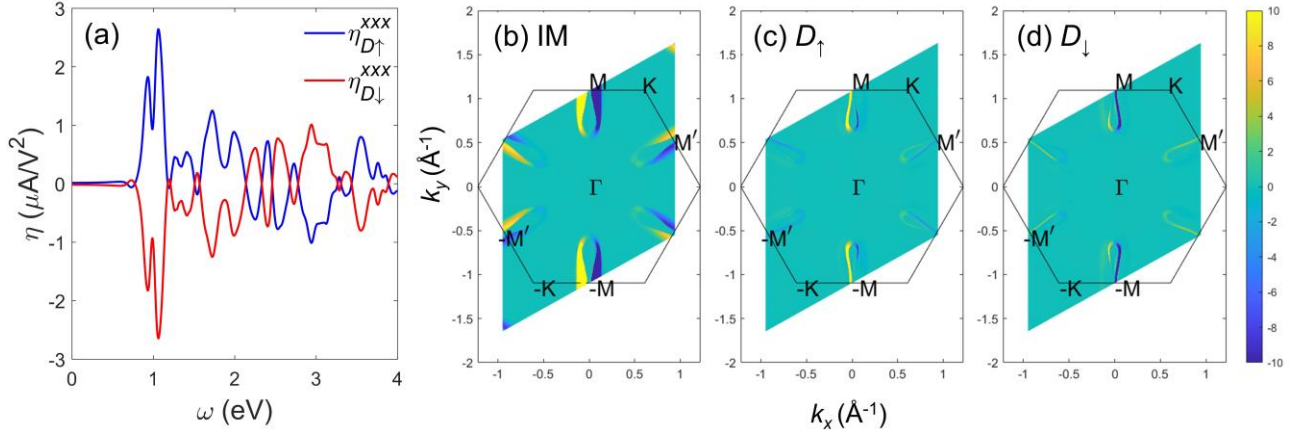


Figure 4. (a) MIC for D_\uparrow and D_\downarrow $\mathbf{L} \parallel \hat{\mathbf{z}}$ bilayer VSe₂ under x -LPL. (b-d) The quantum metric dipole ($\Delta_{nm}^x g_{nm}^{xx}$) ridges in the first BZ, which mainly corresponds to the electronic transition between the VB-3 and the lowest CB for (b) IM, (c) D_\uparrow , and (d) D_\downarrow bilayer VSe₂. The main contribution to the η^{xxx} is around M , under an incident photon energy of 1 eV.

Both the magnetic and electric dipole controlled BPV currents are also evidenced in the T-FeCl₂ and CrI₃ MSFE⁷⁸ systems. The relevant results are provided in Figures S9–S11 and S12, respectively. The out-of-plane easy axis of CrI₃ guarantees its belonging to the magnetic Ising model. In addition, it should be noted that our results are distinct from the \mathcal{PT} -symmetric cases in e.g., Ref. 35, where they showed that the MIC of MnBi₂Te₄ can be tuned by \mathcal{T} and the NSC is switched by the out-of-plane electric field. Similarly, it has been demonstrated that shift current in twisted double bilayer graphene can be switched by the out-of-plane gate voltage which breaks the \mathcal{C}_{2x} symmetry.⁷⁹

In summary, we investigate the LPL illuminated NLO responses in the hexagonal MSFE

bilayers. Our symmetric analyses suggest that the NSC is unaffected by spin polarization, while the MIC photoconductivity is sensitive to the magnetic orientations. In this way, both magnetic and electric dipole could be utilized to control the BPV effect. Our first-principles results confirm these symmetric analyses on two different types of MSFE, bilayers H-VSe₂ and T-FeCl₂. The D_z and SOC controlled valley polarization is captured by a simple $\mathbf{k}\cdot\mathbf{p}$ model, which elucidates the fundamental mechanism of nonvanishing MIC photoconductivity in MSFEs. Considering the profusion of 2D materials with the honeycomb lattice, magnetic configuration dependent photocurrent could find their potential applications in both optospintronic and optoelectronic devices.

Methods.

The DFT calculations on geometric and electronic calculations are performed within the Vienna *ab initio* simulation package (VASP)⁸⁰⁻⁸², using the projector augmented-wave (PAW) method⁸³ to treat the core electrons. A planewave basis set with a kinetic cutoff energy of 500 eV is used to describe the valence electrons. Generalized gradient approximation (GGA) in the form of Perdew-Burke-Ernzerhof (PBE) is applied to treat the exchange-correlation functional,⁸⁴ and the Hubbard U correction is adopted to treat the strong correlation in the magnetic d orbitals. The effective Hubbard U parameter is chosen to be 1.2 eV for the V- d and 4 eV for the Fe- d orbital, which have been proven to give results well consistent with experimental observations. Spin-orbit coupling (SOC) is added self-consistently throughout the calculations. A vacuum region of over 15 Å along the z direction is adopted to eliminate the artificial interactions between different images. The BZ integration is sampled by using Γ -centered Monkhorst–Pack \mathbf{k} -point meshes with grid of (11×11×1). The vdW interactions are semi-empirically described according to the DFT-D3 method.⁸⁵ We use Wannier90 code⁸⁶⁻⁸⁷ to construct the tight-binding model based on the maximally localized Wannier functions (MLWFs). The photo-conductivities are then integrated on a refined \mathbf{k} grid of $500 \times 500 \times 1$, which has been carefully tested to generate well-converged results.

The NSC [$\sigma^{abb}(0; \omega, -\omega)$] and MIC [$\eta^{abb}(0; \omega, -\omega)$] photo-conductivities can be evaluated according to band theory. Here the superscript a refers to current flow direction, and b is the LPL polarization direction. In the length-gauge formulism, they are

$$\sigma^{abb}(0; \omega, -\omega) = \frac{\pi e^3}{\hbar^2} \int \frac{d^3\mathbf{k}}{(2\pi)^3} \sum_{m,n} f_{mn} R_{mn}^{a;b} |r_{mn}^b|^2 \delta(\omega_{mn} - \omega) \quad (5)$$

$$\eta^{abb}(0; \omega, -\omega) = -\frac{\pi e^3}{2\hbar^2} \int \frac{d^3\mathbf{k}}{(2\pi)^3} \sum_{m,n} f_{mn} \Delta_{mn}^a |r_{mn}^b|^2 \delta(\omega_{mn} - \omega) \quad (6)$$

where the sum is over the band indices m and n . The integration is performed in the first BZ, which includes vacuum space contribution in the supercell. In order to correct this and keep the

photocurrent unit consistent with conventional 3D bulk systems, we use the well-adopted scaling approach by multiply a factor $\frac{L_z}{d_{\text{eff}}}$ onto the supercell results. Here L_z is the lattice constant along the z -axis (including vacuum), and d_{eff} is the effective thickness of the system. $f_{mn} = f_{m\mathbf{k}} - f_{n\mathbf{k}}$ is the difference of Fermi-Dirac occupation between bands. The broadening factor of the Dirac delta function is taken to be 0.04 eV. The shift vector $R_{mn}^{a;b}$ is defined as

$$R_{mn}^{a;b} = \partial_a \phi_{mn}^b - A_{mm}^a + A_{nn}^a. \quad (7)$$

Here, ϕ_{mn}^b is the phase of r_{mn}^b ($= |r_{mn}^b| e^{i\phi_{mn}^b}$), and A_{mm}^a is the intraband Berry connection $A_{mm}^a = i\langle m | \partial_a m \rangle$. The $|r_{mn}^b|^2 \delta(\omega_{nm} - \omega)$ evaluates the absorption rate from band m to band n , according to the Fermi's golden rule. $\Delta_{nm}^a = v_{nn}^a - v_{mm}^a$ is the group velocity difference between the n -th and the m -th bands. The explicit \mathbf{k} -dependence on these quantities is omitted.

Under LPL, Eq. (6) is equivalent to the contribution from quantum metric tensor $g_{nm}^{bb} = \sum_{\mu, \nu} \text{Re} \left(r_{m\nu}^b r_{n\mu}^b \right)$, where μ, ν represent the degenerate bands arising from the potential Kramers degeneracy (for example in AFM configurations),³⁴

$$\eta^{a,bb}(0; \omega, -\omega) = -\frac{\tau\pi e^3}{2\hbar^2} \int \frac{d^3\mathbf{k}}{(2\pi)^3} f_{mn} \Delta_{mn}^a (2g_{mn}^{bb}) \delta(\omega_{mn} - \omega) \quad (8)$$

Accordingly, the MIC arises from an excitation between m and n , where g_{nm}^{bb} is weighted by the asymmetric group velocity difference Δ_{nm}^a at the time-reversed $\pm\mathbf{k}$ pairs. The $\Delta_{nm}^a g_{nm}^{bb}$ is defined as quantum metric dipole.⁸⁸

Associated content

Supporting Information: The Supporting Information is available free of charge at

<https://pubs.acs.org/doi/.....>

Energy comparison for different magnetic configurations; The explicit reason for the valley polarization in $\mathbf{L} \parallel \hat{\mathbf{z}}$ D_{\uparrow} and D_{\downarrow} bilayer VSe₂; The symmetry analyses of the allowed photoconductivity for FM bilayer VSe₂; The asymmetric bands associated nonvanishing MIC; The angle dependence of total MAE for MSFE VSe₂; Switchable MAE in bilayer H-VSe₂; Frequency-dependent MIC responses of FM bilayer VSe₂; Quantum metric, velocity, and quantum metric dipole distributions in the first BZ; The NSC for all magnetic configurations; The photocurrent analyses for T-FeCl₂ MSFE; Photocurrent in trilayer cases; Switchable photocurrent in CrI₃ MSFE.

Data availability

All the data and methods are present in the main text and the Supporting Information. Any other relevant data are available from the authors upon reasonable request.

Notes

The authors declare no competing financial interest.

"This document is the unedited author's version of a Submitted Work that was subsequently accepted for publication in Nano Letters, copyright © American Chemical Society after peer review. To access the final edited and published work, see Nano Letters website."

Acknowledgement

We acknowledge the financial support from the National Natural Science Foundation of China (NSFC) under Grant Nos. 12004306, 11974270, 21903063, 12274342, and 11974277.

References

1. Belinicher, V.; Ivchenko, E.; Sturman, B., Kinetic Theory of the Displacement Photovoltaic Effect in Piezoelectrics. *Zh Eksp Teor Fiz* **1982**, *83*, 649-661.
2. Kristoffel, N.; Von Baltz, R.; Hornung, D., On the Intrinsic Bulk Photovoltaic Effect: Performing the Sum over Intermediate States. *Zeitschrift für Physik B Condens. Matt.* **1982**, *47*, 293-296.
3. Sipe, J.; Shkrebtii, A., Second-Order Optical Response in Semiconductors. *Phys. Rev. B* **2000**, *61*, 5337.
4. Yang, M.-M.; Kim, D. J.; Alexe, M., Flexo-Photovoltaic Effect. *Science* **2018**, *360*, 904-907.
5. Morimoto, T.; Nagaosa, N., Topological Nature of Nonlinear Optical Effects in Solids. *Sci. Adv.* **2016**, *2*, e1501524.
6. Tan, L. Z.; Rappe, A. M., Enhancement of the Bulk Photovoltaic Effect in Topological Insulators. *Phys. Rev. Lett.* **2016**, *116*, 237402.
7. Qian, C.; Yu, C.; Jiang, S.; Zhang, T.; Gao, J.; Shi, S.; Pi, H.; Weng, H.; Lu, R., The Role of Shift Vector in High Harmonic Generation from Non-Centrosymmetric Topological Insulators under Strong Laser Fields. *Phys. Rev. X* **2022**, *12*, 021030.
8. Pan, Y.; Zhou, J., Toggling Valley-Spin Locking and Nonlinear Optical Properties of Single-Element Multiferroic Monolayers Via Light. *Phys. Rev. Appl.* **2020**, *14*, 014024.
9. de Juan, F.; Grushin, A. G.; Morimoto, T.; Moore, J. E., Quantized Circular Photogalvanic Effect in Weyl Semimetals. *Nat. Commun.* **2017**, *8*, 15995.
10. Sodemann, I.; Fu, L., Quantum Nonlinear Hall Effect Induced by Berry Curvature Dipole in Time-Reversal Invariant Materials. *Phys. Rev. Lett.* **2015**, *115*, 216806.
11. Dai, Z.; Schankler, A. M.; Gao, L.; Tan, L. Z.; Rappe, A. M., Phonon-Assisted Ballistic Current from First-Principles Calculations. *Phys. Rev. Lett.* **2021**, *126*, 177403.
12. Sotome, M.; Nakamura, M.; Fujioka, J.; Ogino, M.; Kaneko, Y.; Morimoto, T.; Zhang, Y.; Kawasaki, M.; Nagaosa, N.; Tokura, Y., Spectral Dynamics of Shift Current in Ferroelectric Semiconductor SbSi. *Proc. Natl. Acad. Sci. U.S.A.* **2019**, *116*, 1929-1933.
13. Koch, W.; Munser, R.; Ruppel, W.; Würfel, P., Bulk Photovoltaic Effect in BaTiO₃. *Solid State*

Commun. **1975**, *17*, 847-850.

14. Ji, W.; Yao, K.; Liang, Y. C., Evidence of Bulk Photovoltaic Effect and Large Tensor Coefficient in Ferroelectric BiFeO₃ Thin Films. *Phys. Rev. B* **2011**, *84*, 094115.
15. Young, S. M.; Rappe, A. M., First Principles Calculation of the Shift Current Photovoltaic Effect in Ferroelectrics. *Phys. Rev. Lett.* **2012**, *109*, 116601.
16. Chang, K.; Liu, J.; Lin, H.; Wang, N.; Zhao, K.; Zhang, A.; Jin, F.; Zhong, Y.; Hu, X.; Duan, W., Discovery of Robust in-Plane Ferroelectricity in Atomic-Thick SnTe. *Science* **2016**, *353*, 274-278.
17. Xue, F.; Hu, W.; Lee, K. C.; Lu, L. S.; Zhang, J.; Tang, H. L.; Han, A.; Hsu, W. T.; Tu, S.; Chang, W. H., Room-Temperature Ferroelectricity in Hexagonally Layered α -In₂Se₃ Nanoflakes Down to the Monolayer Limit. *Adv. Funct. Mater.* **2018**, *28*, 1803738.
18. Liu, F.; You, L.; Seyler, K. L.; Li, X.; Yu, P.; Lin, J.; Wang, X.; Zhou, J.; Wang, H.; He, H., Room-Temperature Ferroelectricity in CuInP₂S₆ Ultrathin Flakes. *Nat. Commun.* **2016**, *7*, 112357.
19. Wang, H.; Liu, Z.; Yoong, H.; Paudel, T. R.; Xiao, J.; Guo, R.; Lin, W.; Yang, P.; Wang, J.; Chow, G., Direct Observation of Room-Temperature out-of-Plane Ferroelectricity and Tunneling Electroresistance at the Two-Dimensional Limit. *Nat. Commun.* **2018**, *9*, 3319.
20. Yuan, S.; Luo, X.; Chan, H. L.; Xiao, C.; Dai, Y.; Xie, M.; Hao, J., Room-Temperature Ferroelectricity in MoTe₂ Down to the Atomic Monolayer Limit. *Nat. Commun.* **2019**, *10*, 1775.
21. Liang, Y.; Mao, N.; Dai, Y.; Kou, L.; Huang, B.; Ma, Y., Intertwined Ferroelectricity and Topological State in Two-Dimensional Multilayer. *npj Comput. Mater.* **2021**, *7*, 172.
22. Yang, Q.; Wu, M.; Li, J., Origin of Two-Dimensional Vertical Ferroelectricity in WTe₂ Bilayer and Multilayer. *J. Phys. Chem. Lett.* **2018**, *9*, 7160-7164.
23. Li, L.; Wu, M., Binary Compound Bilayer and Multilayer with Vertical Polarizations: Two-Dimensional Ferroelectrics, Multiferroics, and Nanogenerators. *ACS nano* **2017**, *11*, 6382-6388.
24. Wu, M.; Li, J., Sliding Ferroelectricity in 2D Van der Waals Materials: Related Physics and Future Opportunities. *Proc. Natl. Acad. Sci. U.S.A.* **2021**, *118*, e2115703118.
25. Ding, N.; Chen, J.; Gui, C.; You, H.; Yao, X.; Dong, S., Phase Competition and Negative Piezoelectricity in Interlayer-Sliding Ferroelectric ZrI₂. *Phys. Rev. Mater.* **2021**, *5*, 084405.
26. Zhong, T.; Ren, Y.; Zhang, Z.; Gao, J.; Wu, M., Sliding Ferroelectricity in Two-Dimensional MoA₂N₄ (A= Si or Ge) Bilayers: High Polarizations and Moiré Potentials. *J. Mater. Chem. A* **2021**, *9*, 19659-19663.
27. Rogée, L.; Wang, L.; Zhang, Y.; Cai, S.; Wang, P.; Chhowalla, M.; Ji, W.; Lau, S. P., Ferroelectricity in Untwisted Heterobilayers of Transition Metal Dichalcogenides. *Science* **2022**, *376*, 973-978.
28. Xiao, J.; Wang, Y.; Wang, H.; Pemmaraju, C.; Wang, S.; Muscher, P.; Sie, E. J.; Nyby, C. M.; Devereaux, T. P.; Qian, X., Berry Curvature Memory through Electrically Driven Stacking Transitions. *Nat. Phys.* **2020**, *16*, 1028-1034.
29. Xiao, R.-C.; Gao, Y.; Jiang, H.; Gan, W.; Zhang, C.; Li, H., Switchable and Unswitchable Bulk Photovoltaic Effect in Two-Dimensional Interlayer-Sliding Ferroelectrics. *npj Comput. Mater.* **2022**, *8*, 138.
30. Eerenstein, W.; Mathur, N.; Scott, J. F., Multiferroic and Magnetoelectric Materials. *Nature* **2006**, *442*, 759-765.
31. Scott, J., Multiferroic Memories. *Nat. Mater.* **2007**, *6*, 256-257.
32. Zhang, Y.; Holder, T.; Ishizuka, H.; de Juan, F.; Nagaosa, N.; Felser, C.; Yan, B., Switchable Magnetic Bulk Photovoltaic Effect in the Two-Dimensional Magnet CrI₃. *Nat. Commun.* **2019**, *10*, 3783.
33. Holder, T.; Kaplan, D.; Yan, B., Consequences of Time-Reversal-Symmetry Breaking in the

- Light-Matter Interaction: Berry Curvature, Quantum Metric, and Adiabatic Motion. *Phys. Rev. Res.* **2020**, *2*, 033100.
34. Chen, H.; Ye, M.; Zou, N.; Gu, B.-L.; Xu, Y.; Duan, W., Basic Formulation and First-Principles Implementation of Nonlinear Magneto-Optical Effects. *Phys. Rev. B* **2022**, *105*, 075123.
35. Wang, H.; Qian, X., Electrically and Magnetically Switchable Nonlinear Photocurrent in PT-Symmetric Magnetic Topological Quantum Materials. *npj Comput. Mater.* **2020**, *6*, 199.
36. Fei, R.; Song, W.; Pusey-Nazzaro, L.; Yang, L., PT-Symmetry-Enabled Spin Circular Photogalvanic Effect in Antiferromagnetic Insulators. *Phys. Rev. Lett.* **2021**, *127*, 207402.
37. Ma, Y.; Dai, Y.; Guo, M.; Niu, C.; Zhu, Y.; Huang, B., Evidence of the Existence of Magnetism in Pristine VX₂ Monolayers (X= S, Se) and Their Strain-Induced Tunable Magnetic Properties. *ACS Nano* **2012**, *6*, 1695-1701.
38. Bonilla, M.; Kolekar, S.; Ma, Y.; Diaz, H. C.; Kalappattil, V.; Das, R.; Eggers, T.; Gutierrez, H. R.; Phan, M.-H.; Batzill, M., Strong Room-Temperature Ferromagnetism in VSe₂ Monolayers on Van der Waals Substrates. *Nat. Nanotechnol.* **2018**, *13*, 289-293.
39. Zhang, W.-B.; Qu, Q.; Zhu, P.; Lam, C.-H., Robust Intrinsic Ferromagnetism and Half Semiconductivity in Stable Two-Dimensional Single-Layer Chromium Trihalides. *J. Mater. Chem. C* **2015**, *3*, 12457-12468.
40. Liu, J.; Sun, Q.; Kawazoe, Y.; Jena, P., Exfoliating Biocompatible Ferromagnetic Cr-Trihalide Monolayers. *Phys. Chem. Chem. Phys.* **2016**, *18*, 8777-8784.
41. Huang, B.; Clark, G.; Navarro-Moratalla, E.; Klein, D. R.; Cheng, R.; Seyler, K. L.; Zhong, D.; Schmidgall, E.; McGuire, M. A.; Cobden, D. H., Layer-Dependent Ferromagnetism in a Van der Waals Crystal Down to the Monolayer Limit. *Nature* **2017**, *546*, 270-273.
42. Zhuang, H. L.; Kent, P.; Hennig, R. G., Strong Anisotropy and Magnetostriction in the Two-Dimensional Stoner Ferromagnet Fe₃GeTe₂. *Phys. Rev. B* **2016**, *93*, 134407.
43. Deng, Y.; Yu, Y.; Song, Y.; Zhang, J.; Wang, N. Z.; Sun, Z.; Yi, Y.; Wu, Y. Z.; Wu, S.; Zhu, J., Gate-Tunable Room-Temperature Ferromagnetism in Two-Dimensional Fe₃GeTe₂. *Nature* **2018**, *563*, 94-99.
44. Chen, S.; Wu, F.; Li, Q.; Sun, H.; Ding, J.; Huang, C.; Kan, E., Prediction of Room-Temperature Ferromagnetism in a Two-Dimensional Direct Band Gap Semiconductor. *Nanoscale* **2020**, *12*, 15670-15676.
45. Ye, C.; Wang, C.; Wu, Q.; Liu, S.; Zhou, J.; Wang, G.; Soll, A.; Sofer, Z.; Yue, M.; Liu, X., Layer-Dependent Interlayer Antiferromagnetic Spin Reorientation in Air-Stable Semiconductor CrSBr. *ACS nano* **2022**, *16*, 11876-11883.
46. Kan, M.; Adhikari, S.; Sun, Q., Ferromagnetism in MnX₂ (X= S, Se) Monolayers. *Phys. Chem. Chem. Phys.* **2014**, *16*, 4990-4994.
47. O'Hara, D. J.; Zhu, T.; Trout, A. H.; Ahmed, A. S.; Luo, Y. K.; Lee, C. H.; Brenner, M. R.; Rajan, S.; Gupta, J. A.; McComb, D. W., Room Temperature Intrinsic Ferromagnetism in Epitaxial Manganese Selenide Films in the Monolayer Limit. *Nano Lett.* **2018**, *18*, 3125-3131.
48. Wu, M., Two-Dimensional Van Der Waals Ferroelectrics: Scientific and Technological Opportunities. *ACS nano* **2021**, *15*, 9229-9237.
49. Yasuda, K.; Wang, X.; Watanabe, K.; Taniguchi, T.; Jarillo-Herrero, P., Stacking-Engineered Ferroelectricity in Bilayer Boron Nitride. *Science* **2021**, *372*, 1458-1462.
50. Vizner Stern, M.; Waschitz, Y.; Cao, W.; Nevo, I.; Watanabe, K.; Taniguchi, T.; Sela, E.; Urbakh, M.; Hod, O.; Ben Shalom, M., Interfacial Ferroelectricity by Van der Waals Sliding. *Science* **2021**, *372*, 1462-1466.
51. Wang, X.; Yasuda, K.; Zhang, Y.; Liu, S.; Watanabe, K.; Taniguchi, T.; Hone, J.; Fu, L.; Jarillo-

- Herrero, P., Interfacial Ferroelectricity in Rhombohedral-Stacked Bilayer Transition Metal Dichalcogenides. *Nat. Nanotechnol.* **2022**, *17*, 367-371.
52. Yu, B.-W.; Liu, B.-G., Possible Structural and Bond Reconstruction in 2d Ferromagnetic Semiconductor VSe₂ under Uniaxial Stress. *Nanotechnology* **2022**, *33*, 455706.
53. Zhang, H.; Liu, L.-M.; Lau, W.-M., Dimension-Dependent Phase Transition and Magnetic Properties of VS₂. *J. Mater. Chem. A* **2013**, *1*, 10821-10828.
54. Torun, E.; Sahin, H.; Singh, S.; Peeters, F., Stable Half-Metallic Monolayers of FeCl₂. *Appl. Phys. Lett.* **2015**, *106*, 192404.
55. Liu, X.; Pyatakov, A. P.; Ren, W., Magnetolectric Coupling in Multiferroic Bilayer VS₂. *Phys. Rev. Lett.* **2020**, *125*, 247601.
56. Zhang, T.; Xu, X.; Huang, B.; Dai, Y.; Ma, Y., 2D Spontaneous Valley Polarization from Inversion Symmetric Single-Layer Lattices. *npj Comput. Mater.* **2022**, *8*, 64.
57. Fei, Z.; Zhao, W.; Palomaki, T. A.; Sun, B.; Miller, M. K.; Zhao, Z.; Yan, J.; Xu, X.; Cobden, D. H., Ferroelectric Switching of a Two-Dimensional Metal. *Nature* **2018**, *560*, 336-339.
58. Ding, W.; Zhu, J.; Wang, Z.; Gao, Y.; Xiao, D.; Gu, Y.; Zhang, Z.; Zhu, W., Prediction of Intrinsic Two-Dimensional Ferroelectrics in In₂Se₃ and Other III₂-VI₃ Van der Waals Materials. *Nat. Commun.* **2017**, *8*, 14956.
59. Tong, W.-Y.; Gong, S.-J.; Wan, X.; Duan, C.-G., Concepts of Ferrovalley Material and Anomalous Valley Hall Effect. *Nat. Commun.* **2016**, *7*, 13612.
60. Ahamd, H.; Zhou, J., Intercalation Induced Ferromagnetism in Group-V Transition Metal Dichalcogenide Bilayer. *AIP Adv.* **2020**, *10*, 045323.
61. Takashina, K.; Ono, Y.; Fujiwara, A.; Takahashi, Y.; Hirayama, Y., Valley Polarization in Si (100) at Zero Magnetic Field. *Phys. Rev. Lett.* **2006**, *96*, 236801.
62. Renard, V.; Piot, B.; Waintal, X.; Fleury, G.; Cooper, D.; Niida, Y.; Tregurtha, D.; Fujiwara, A.; Hirayama, Y.; Takashina, K., Valley Polarization Assisted Spin Polarization in Two Dimensions. *Nat. Commun.* **2015**, *6*, 7230.
63. Zhao, C.; Norden, T.; Zhang, P.; Zhao, P.; Cheng, Y.; Sun, F.; Parry, J. P.; Taheri, P.; Wang, J.; Yang, Y., Enhanced Valley Splitting in Monolayer WSe₂ Due to Magnetic Exchange Field. *Nat. Nanotechnol.* **2017**, *12*, 757-762.
64. Yuan, H.; Bahramy, M. S.; Morimoto, K.; Wu, S.; Nomura, K.; Yang, B.-J.; Shimotani, H.; Suzuki, R.; Toh, M.; Kloc, C., Zeeman-Type Spin Splitting Controlled by an Electric Field. *Nat. Phys.* **2013**, *9*, 563-569.
65. Moore, J. E.; Orenstein, J., Confinement-Induced Berry Phase and Helicity-Dependent Photocurrents. *Phys. Rev. Lett.* **2010**, *105*, 026805.
66. Morimoto, T.; Nagaosa, N., Topological Nature of Nonlinear Optical Effects in Solids. *Sci. Adv.* **2016**, *2*, e1501524.
67. Ahn, J.; Guo, G.-Y.; Nagaosa, N., Low-Frequency Divergence and Quantum Geometry of the Bulk Photovoltaic Effect in Topological Semimetals. *Phys. Rev. X* **2020**, *10*, 041041.
68. Zhang, C.; Pi, H.; Zhou, L.; Li, S.; Zhou, J.; Du, A.; Weng, H., Switchable Topological Phase Transition and Nonlinear Optical Properties in a ReC₂H Monolayer. *Phys. Rev. B* **2022**, *105*, 245108.
69. Wang, H.; Qian, X., Ferroelectric Nonlinear Anomalous Hall Effect in Few-Layer WTe₂. *npj Comput. Mater.* **2019**, *5*, 119.
70. Mu, X.; Pan, Y.; Zhou, J., Pure Bulk Orbital and Spin Photocurrent in Two-Dimensional Ferroelectric Materials. *npj Comput. Mater.* **2021**, *7*, 61.
71. Bedoya-Pinto, A.; Ji, J.-R.; Pandeya, A. K.; Gargiani, P.; Valvidares, M.; Sessi, P.; Taylor, J. M.; Radu, F.; Chang, K.; Parkin, S. S., Intrinsic 2D-XY Ferromagnetism in a Van der Waals Monolayer.

Science **2021**, *374*, 616-620.

72. Zhou, J., Photo-Magnetization in Two-Dimensional Sliding Ferroelectrics. *npj 2D Mater. Appl.* **2022**, *6*, 15.

73. Edelstein, V. M., Spin Polarization of Conduction Electrons Induced by Electric Current in Two-Dimensional Asymmetric Electron Systems. *Solid State Commun.* **1990**, *73*, 233-235.

74. Li, X.; Chen, H.; Niu, Q., Out-of-Plane Carrier Spin in Transition-Metal Dichalcogenides under Electric Current. *Proc. Natl. Acad. Sci. U.S.A.* **2020**, *117*, 16749-16755.

75. Schankler, A. M.; Gao, L.; Rappe, A. M., Large Bulk Piezophotovoltaic Effect of Monolayer 2 H-MoS₂. *J. Phys. Chem. Lett.* **2021**, *12*, 1244-1249.

76. Zhou, X.; Van Driel, H.; Mak, G., Femtosecond Kinetics of Photoexcited Carriers in Germanium. *Phys. Rev. B* **1994**, *50*, 5226.

77. Sjakste, J.; Tanimura, K.; Barbarino, G.; Perfetti, L.; Vast, N., Hot Electron Relaxation Dynamics in Semiconductors: Assessing the Strength of the Electron-Phonon Coupling from the Theoretical and Experimental Viewpoints. *J. Phys.: Condens. Matter* **2018**, *30*, 353001.

78. Chen, W.; Sun, Z.; Wang, Z.; Gu, L.; Xu, X.; Wu, S.; Gao, C., Direct Observation of Van Der Waals Stacking-Dependent Interlayer Magnetism. *Science* **2019**, *366*, 983-987.

79. Ma, C.; Yuan, S.; Cheung, P.; Watanabe, K.; Taniguchi, T.; Zhang, F.; Xia, F., Intelligent Infrared Sensing Enabled by Tunable Moiré Quantum Geometry. *Nature* **2022**, *604*, 266-272.

80. Kresse, G.; Hafner, J., Ab Initio Molecular Dynamics for Liquid Metals. *Phys. Rev. B* **1993**, *47*, 558.

81. Kresse, G.; Furthmüller, J., Efficient Iterative Schemes for Ab Initio Total-Energy Calculations Using a Plane-Wave Basis Set. *Phys. Rev. B* **1996**, *54*, 11169.

82. Blöchl, P. E., Projector Augmented-Wave Method. *Phys. Rev. B* **1994**, *50*, 17953.

83. Blöchl, P., Generalized Gradient Approximation Made Simple. *Phys. Rev. B: Condens. Matter Mater. Phys.* **1994**, *50*, 17953.

84. Perdew, J. P.; Burke, K.; Ernzerhof, M., Generalized Gradient Approximation Made Simple. *Phys. Rev. Lett.* **1996**, *77*, 3865.

85. Grimme, S., Semiempirical Gga-Type Density Functional Constructed with a Long-Range Dispersion Correction. *J. Comput. Chem.* **2006**, *27*, 1787-1799.

86. Mostofi, A. A.; Yates, J. R.; Pizzi, G.; Lee, Y.-S.; Souza, I.; Vanderbilt, D.; Marzari, N., An Updated Version of Wannier90: A Tool for Obtaining Maximally-Localised Wannier Functions. *Comput. Phys. Commun.* **2014**, *185*, 2309-2310.

87. Mostofi, A. A.; Yates, J. R.; Lee, Y.-S.; Souza, I.; Vanderbilt, D.; Marzari, N., Wannier90: A Tool for Obtaining Maximally-Localised Wannier Functions. *Comput. Phys. Commun.* **2008**, *178*, 685-699.

88. Wang, C.; Gao, Y.; Xiao, D., Intrinsic Nonlinear Hall Effect in Antiferromagnetic Tetragonal Cumnas. *Phys. Rev. Lett.* **2021**, *127*, 277201.